

High resolution terahertz ATR frequency-domain spectroscopy for monitoring spinal cord injury in rats

XING FANG,^{1,3,†} HANXU HUANG,^{2,†} HONGQI ZHANG,¹ ZUOMIN YANG,¹ ZHIDONG LYU,¹ HANG YANG,¹ NAN LI,¹ TENGFEI ZHAO,² XIANBIN YU,^{1,4}  AND LU ZHANG^{1,5} 

¹ College of Information Science and Electronic Engineering, Zhejiang University, Hangzhou 310027, China

² Department of Orthopedic Surgery, Second Affiliated Hospital of Zhejiang University School of Medicine, Hangzhou 310009, China

³ xingfang@zju.edu.cn

⁴ xyu@zju.edu.cn

⁵ zhanglu1993@zju.edu.cn

[†] These authors contributed equally to this work.

Abstract: Traumatic spinal cord injury (SCI) can lead to permanent neurological impairment, underscoring the urgency of regular therapeutic intervention and monitoring. In this study, we propose a new strategy for monitoring spinal cord injury through serum based on high-resolution THz attenuated total reflection frequency domain spectroscopy (THz-ATR-FDS). We demonstrated serum spectral differences at different time points after experimental SCI in rats. We also studied the relationship between serum lipid concentration and the time of SCI, which revealed the potential of lipid molecules as biomarkers of SCI. In addition, based on the principal component analysis (PCA) and least squares regression (LSR) models, the quantitative relationship between the refractive index spectrum and lipid concentration in serum was automatically analyzed. This work highlights terahertz spectroscopy as a promising tool for label-free, periodic, and efficient monitoring of SCI.

© 2023 Optica Publishing Group under the terms of the [Optica Open Access Publishing Agreement](#)

1. Introduction

Spinal cord injury (SCI) stands as a neurological disorder culminating in enduring deficits within the nervous system and profound impairment of motor function [1]. Based on its etiology, SCI can be categorized into traumatic and nontraumatic origins [2]. SCI has garnered the status of a global health concern, with recent statistical data revealing that upwards of 27 million individuals across the globe grapple with enduring incapacities due to traumatic SCI [3]. The mechanisms of traumatic SCI are intricate and distinct, delineated across acute, subacute, intermediate, and chronic phases [4]. Over the preceding two decades, the numerous nerve repair and regeneration technologies for SCI shifted from preclinical investigation to clinical trial phases [5–7]. However, the expeditious and label-free monitoring of the severity and neurological recovery of SCI remains a pivotal technological bottleneck in the realm of neurosurgical diagnosis and treatment.

The existing methods for monitoring and assessing SCI can be classified into three categories. The first is neurological examination, which involves assessing a patient's motor ability and sensory function through clinical observation. This method is relatively simple and non-invasive, but due to its subjective nature, it has lower objectivity and specificity. The second category includes imaging examinations such as X-ray [8], CT scans [9], and MRI [10]. These methods provide powerful imaging tools for direct observation of the site of injury in SCI patients and are crucial for assessing patient prognosis, which can give much more specific information

about spinal cord injury. However, imaging methods lack of analysis of molecular levels and physiological indicators in patients, needing to be used in combination with other biochemical screening methods. The third category comprises electrophysiological examinations, which assess the integrity of the nervous system by recording the electrophysiological characteristics of SCI patients' bodies. This method provides objective physiological indicators by measuring the actual electrical activity within the body. However, electrophysiological measurements lack consistent measurement standards for different SCI patients, which can lead to diagnostic differences [11].

In recent years, the research on biomarkers has aroused great interest in academic circles. Biomarkers are objective indicators that can measure normal biological processes, pathological processes, and drug responses. Research on biomarkers in serum and cerebrospinal fluid can reveal the biological mechanisms of neuronal damage, monitor the severity of injury, and potentially predict the recovery of neurological function in spinal cord injury (SCI) patients. Currently, the most recommended SCI biomarkers are neuron or astrocyte-related proteins, such as GFAP, S100 β , and ubiquitin C-terminal hydrolase L1 (UCH-L1) [12]. However, they may not penetrate the blood-brain barrier and can be relatively complex and expensive to detect. Recent studies have shown that during SCI, certain molecules, including hemolytic lipids [13,14], are involved in the inflammatory processes during secondary injury. Lipid metabolites are of particular interest as potential biomarkers during spinal cord injury due to their high lipid content and susceptibility to oxidative damage in the spinal cord [15]. Among these, glycerophospholipids (GP) and triglycerides (TG) are the most noteworthy. In the acute phase of spinal cord injury, endothelial cells and astrocytes become reactive, leading to the dysfunction of various inflammatory cytokines such as tumor necrosis factor (TNF)- α and interleukins (IL-1 α , IL-6, and IL-1 β), which in turn promote changes in blood-spinal cord barrier (BSCB) permeability. This allows lipid molecules like GP and TG to penetrate the blood-spinal cord barrier, resulting in an increase in their concentrations in the blood [16]. Therefore, exploring the use of GP and TG as biomarkers to monitor the pathological processes of SCI is of great importance. While selecting lipid molecules as biomarkers may lack specificity since conditions other than spinal cord injury, such as obesity, diabetes, atherosclerosis, and hypothyroidism, can also lead to elevated blood lipid concentrations, in the majority of clinical cases, GP and TG molecule concentrations have a positive correlation with the degree and time of spinal cord injury [17]. This offers a new approach for continuous monitoring of the pathology of spinal cord injury. Currently, due to the typical small sample size in SCI, a combination of multiple biomarkers is often chosen to establish the relationship between biomarkers and clinical conditions [18], and research on GP and TG molecules will provide new avenues for the selection of various biomarkers.

The THz frequency band, spanning from 0.1 to 10 THz, has recently garnered escalating attention within the biomedical domain attributed to its distinctive characteristics [19]. Notably, THz spectroscopy has emerged as a sensitive technique for discerning the unique molecular fingerprint characteristics inherent in biological specimens. This propensity owes itself to the localization of vibrational and rotational energy states of pivotal biomolecules, such as proteins and lipids, within the confines of the THz frequency range [20], which makes THz spectroscopy a promising technology for monitoring the changes of lipid concentration in patients with SCI. An additional noteworthy feature of THz radiation is its non-ionizing nature. When compared with currently commercialized waves like X-rays, the photon energy carried by THz waves is considerably modest, measuring only a few millielectronvolts. Its low-energy attribute and potential for label-free, periodic, and non-destructive diagnosis make it a valuable tool for identifying and monitoring traumatic spinal cord injury cases [21]. The use of THz spectroscopy for SCI diagnosis allows for periodic and non-destructive monitoring of patients' conditions

over time. This can be particularly useful for tracking the progress of treatment and recovery in patients with SCI.

According to the different types of terahertz sources, THz spectroscopy can be classified into pulse wave domain spectroscopy (TDS) and continuous wave frequency domain spectroscopy (FDS). THz-TDS schemes rely on complex femtosecond lasers and optical delay lines to generate and sample broadband terahertz pulses [22]. To date, the great majority of THz spectroscopy has been performed in the time domain. However, spectral detection of SCI requires a faster and more economical scheme, especially for investigating the concentration changes of biomolecules in the process of SCI, which requires higher spectral resolution and freer frequency selective ability, these requirements make FDS a more promising scheme. In recent years, THz-FDS with coherent detection based on photomixing techniques have emerged, which exhibit enhanced frequency resolution (up to 50 MHz) and stability of power, accompanied by more compact system architectures [23]. More importantly, FDS obtains the frequency domain spectral data of any specified frequency band in real-time based on the linear frequency scanning of the tunable laser, which makes it an efficient and economical scheme for real-time and long-term detection of SCI. Traditional terahertz spectroscopy typically operates in either transmission or reflection mode [24,25]. However, THz waves transmitted via polar biomolecules are substantially absorbed, whereas the reflection mode produces diffuse reflection and increases the spatial optical path's calibration complexity. To solve this problem, the attenuated total reflection (ATR) mode has been applied in the terahertz frequency band [26]. The scheme of the ATR mode is based on the principle of total reflection of lights, and the evanescent wave generated by the ATR prism is applied to detect the sample [27]. Compared with the transmission mode and reflection mode, THz spectroscopy systems in ATR mode can detect highly absorbing samples sensitively without the need for complicated sample pretreatment and replacement processes, which makes it a system structure well suited for biological spectrum detection [28].

In this paper, for the first time, we propose photomixing terahertz continuous-wave frequency-domain spectroscopy (THz-FDS) with ATR technology, providing a new strategy for monitoring SCI through THz-ATR-FDS. The SCI model of rats was established by compression methods. After rats suffered experimental SCI exposure through the compression of the calibration clip, spectral differences in serum collected at different time points were studied. At the same time, the pathogenesis of SCI was investigated by tracking variations in the lipid concentration of the serum. We discovered that the concentrations of glycerophospholipids (GP) and triglycerides (TG) in serum increased with injury time and injury degree, which indicates that lipid molecules are important molecular markers in monitoring of SCI. Moreover, based on the THz refractive index spectra of serum, the principal component analysis (PCA) and least squares regression (LSR) algorithms were performed to quantitatively analyze the concentrations of GP and TG. This study demonstrates that terahertz spectroscopy detection can serve as a significant complementary tool for SCI assessment, paving the way for the clinical diagnosis and continuous monitoring of SCI using the THz-ATR-FDS system.

2. Experimental methods

2.1. Experimental setup

The overall system architecture of the THz-ATR-FDS system we built is shown in Fig. 1. The whole system is mainly composed of DFB lasers (Toptica Photonics AG), terahertz photoconductive antennas (TERA15-FC, MenloSystem), off-axis parabolic mirrors (GCC-501101, DHC), an ATR prism, and DAQ electronics. The DFB lasers operate at distinct center wavelengths of 1533 nm and 1538 nm, yielding a maximum output power of 15 dBm while retaining a tunable span of 600 GHz. This coherent scheme engenders continuous-wave terahertz emissions via optical heterodyning with high-bandwidth photoconductors, whereby the output of the dual continuous-wave lasers transmutes into terahertz radiation precisely at the discrepancy frequency

of said lasers. Through the temperature control unit, the frequent difference between the two DFB lasers can be controlled with single megahertz precision; therefore, the solution based on optical mixing can realize a high-resolution terahertz spectrum. Combined with the Hilbert transform method, we achieved a spectrum resolution of 100 MHz and a dynamic range greater than 60 dB. The testing for the dynamic range is conducted in a dark current environment. Initially, we perform a spectral scan, and subsequently, we disconnect the optical fiber connected to the transmitting-end photoconductive antenna to obtain the dark current amplitude of the system. The dynamic range of the system is then calculated by dividing the spectral amplitude by the dark current amplitude. The spatial optical path of the system is mainly composed of an off-axis parabolic mirror and an ATR prism. The terahertz continuous wave generated by the photomixer transmitter is reflected and focused by OPM1 and OPM2, and then enters the ATR prism. On the nether surface of the ATR prism, the terahertz wave undergoes attenuated total reflection, thus giving rise to the genesis of an evanescent wave. Subsequently, the terahertz wave interacts with the sample placed on the surface of the ATR prism, carries information about the sample, and emits in the same direction as the incident wave. After being reflected by OPM3 and OPM4, the THz wave is focused on the photomixer receiver. In the receiver, the THz signal is mixed with the optical beat note of another optical arm. Since there is a delayed self-heterodyne between the two optical beat notes due to different lengths of propagation paths, there is a frequency difference between the THz field and the optical beat note at the receiver. Consequently, the receiver can obtain the intermediate-frequency electrical signal carrying the amplitude and phase information of the terahertz field. The output signal is sent to the lock-in amplifier in DAQ electronics and sampled to obtain the oscillating photocurrent signal. The amplitude and phase information of the spectra can be directly obtained through the Hilbert transform, and the absorption coefficient and refractive index of the sample can be calculated. In our THz-ATR-FDS system, the time required for a single detection is less than 1 minute.

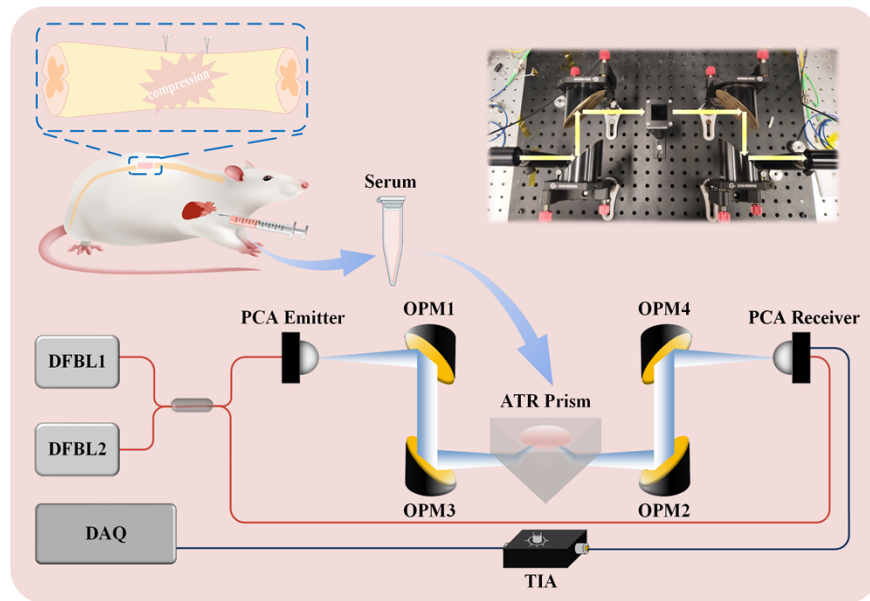


Fig. 1. Schematic diagram of THz-ATR-FDS system and SCI model in rats. DFBL, distributed feedback laser; PCA, photoconductive antenna; OPM, off-axis parabolic mirror; TIA, transimpedance amplifier; LIA, lock-in amplifier; DAQ, data digitization and acquisition electronics. The upper right is the actual spatial optical path of the system, and the upper left is the process of establishing the SCI model.

According to the total reflection theorem, the material and bottom angle of the ATR prism determine the maximum measurable refractive index and the sensitivity of the system, which is related to the attenuated total reflectivity and penetration depth of evanescent waves. After comprehensive consideration, we finally chose the ATR prism made of high-resistance silicon with a base angle of 45° , corresponding to the maximum measurable refractive index of 2.88, attenuated total reflectivity of 0.79, and penetration depth of 0.094 mm. To ensure the accuracy of evanescent wave measurement, the minimum thickness of the sample must be greater than the penetration depth. In this study, the volume of the serum sample measured each time is approximately 100–130 μl , and the sample thickness is greater than 0.3 mm, which meets the needs of the experiment.

2.2. Animals

Adult female Sprague-Dawley rats weighing 200–220 g were kept in a regulated environment, maintained at a stable temperature of around 24°C and a humidity level of about 40%. Their living conditions followed a 12-hour cycle of light and darkness, with regular replacements of food, water, and bedding. All experimental animals were purchased from the Hangzhou Medical College (Zhejiang, China). All animal procedures used in this study were performed in accordance with the China Animal Welfare Legislation.

2.3. SCI model construction and sample preparation

The T10 segments were chosen for evaluation as the highest points of the dorsal spine in rats. After inducing anesthesia through intraperitoneal injection of 1% (w/v) pentobarbital sodium (5 mL/kg). Surgical incision sites were shaved and disinfected using iodine povidone. After an incision in the skin, the fascia was exposed, and the muscles were gently dissected. The paravertebral tissues were then systematically separated layer by layer after an incision in the muscles on either side of the spine, exposing the T10 segments. A laminectomy was carried out to reveal the dura mater. To induce spinal cord injury, compression was applied with a vascular clamp for 30 or 120 seconds (15 g force, Oscar, China). After surgery, the muscle and skin are sutured layer by layer and sterilized with povidone iodine. Postoperative warmth is maintained, and the bladder is emptied twice a day through artificial drainage. The control group underwent identical procedures as described above, but without the SCI construction.

Spinal cord injuries can be categorized based on time into the following phases: acute phase (<12 hours), subacute phase (12 hours to 2 days), intermediate phase (2 days to 7 days), and chronic phase (>7 days). Therefore, in order to investigate the pathological characteristics at different phases, serum was extracted from rat hearts at 6 hours, 1 day, 3 days, 7 days, and 14 days after the spinal cords were compressed in 30s and 120s respectively (3 rats for each group), while a sham group without SCI was set as the control group (number = 6 rats). The rats that were already anesthetized were placed in the supine position, and the area surrounding the raphe was de-haired and disinfected. Following this, the blood collection needle was inserted obliquely into the rat's thoracic cavity beneath the raphe. Once the tip of the needle passed through the diaphragm into the ventricle, the blood (4-5 ml) was collected using a blood collection tube (367955, BD Vacutainer), and the plasma was centrifuged (4000 g, 15 min) to obtain a serum sample (1-2 ml). Then the THz spectra of these sera was measured with the THz-ATR-FDS.

3. Principles

According to the principle of photomixing coherent detection, the photocurrent in the terahertz receiver $I_{ph}(\omega)$ can be expressed as:

$$I_{ph}(\omega) = E_{THz}(\omega) \cos(2\pi\Delta L\omega/c) \quad (1)$$

where E_{THz} is the amplitude of the terahertz electric field, ΔL is the length difference between the transmitter arm and the receiver arm, related to the refractive index of the sample, ω is the frequency of THz waves, and c is the light speed in vacuum. Through the Hilbert transform, the complex form of the photocurrent can be obtained:

$$\tilde{I}_{ph}(\omega) = I_{ph}(\omega) + iH(I_{ph}(\omega)) \quad (2)$$

where H means Hilbert transform, therefore we can easily obtain the ratio of attenuated total coefficient R between the reference signal and the sample signal, which can be expressed as follows:

$$R = \tilde{I}_{sam}(\omega)/\tilde{I}_{ref}(\omega) = (\tilde{I}_{sam}(\omega)/\tilde{I}_{in}(\omega))/(\tilde{I}_{ref}(\omega)/\tilde{I}_{in}(\omega)) = r_{sam}(\omega)/r_{ref}(\omega) \quad (3)$$

where $r_{sam}(\omega)$ denotes the attenuated total coefficient of the sample signal, and $r_{ref}(\omega)$ is the attenuated total coefficient of the reference signal. According to the Fresnel equations of p-polarized radiation, $r_{sam}(\omega)$ and $r_{ref}(\omega)$ satisfy the following equations, respectively.

$$r_{sam} = \frac{n_{prism}^{1/2}(\tilde{n}_{sample} - \tilde{n}_{prism}\sin^2\theta)^{1/2} - \tilde{n}_{sample}\cos\theta}{n_{prism}^{1/2}(\tilde{n}_{sample} - \tilde{n}_{prism}\sin^2\theta)^{1/2} + \tilde{n}_{sample}\cos\theta} \quad (4)$$

$$r_{ref} = \frac{n_{prism}^{1/2}(n_{air} - n_{prism}\sin^2\theta)^{1/2} - n_{air}\cos\theta}{n_{prism}^{1/2}(n_{air} - n_{prism}\sin^2\theta)^{1/2} + n_{air}\cos\theta} = \exp(-0.118i) \quad (5)$$

where $n_{prism} = 3.42$ is the refractive index of Dove prism, $n_{air} = 1$ is the refractive index of air, $\theta = 55.7^\circ$ is the incident angle of THz wave. Through Eq. (3) and Eq. (4), the complex refractive index of sample \tilde{n}_{sample} can be calculated as follows:

$$\tilde{n}_{sample} = n_{prism} \left[\frac{(1 - Rr_{ref})^2 \pm \sqrt{(1 - Rr_{ref})^4 - 4(1 + Rr_{ref})^2(1 - Rr_{ref})^2\cos^2\theta\sin^2\theta}}{2(1 + Rr_{ref})^2\cos^2\theta} \right] \quad (6)$$

Then, the refractive index n_{sam} and absorption coefficient α_{sam} can be expressed as follows:

$$n_{sample} = \text{Re}[\tilde{n}_{sample}] \quad (7)$$

$$\alpha_{sample} = \frac{2\omega\text{Im}[\tilde{n}_{sample}]}{c} \quad (8)$$

4. Results and discussion

4.1. Lipidomics

The relationship between serum lipid concentration and terahertz spectral characteristics was demonstrated. The concentrations of different lipids in the serum samples were measured with a mass spectrometer. Figure 2(a) depicts the concentration of GP and TG. It is obvious that with the increase in injury time and degree, the concentrations of GP and TG are both gradually increasing, which is negatively correlated with the THz refractive index spectra. However, the growing trends of GP and TG differ. To observe the changes in lipid concentration more clearly, we plotted the line graphs of GP and TG concentration over time, as shown in Fig. 2(b) and 2(c) respectively. It can be seen from Fig. 2(b) that the concentration of TG in serum increased dramatically in the acute phase of injury (within 24 hours), while in the subacute phase (1 day–7 days), the concentration of TG did not grow significantly, and then at 14 days, the concentration

of TG increased significantly to 3 times that of 7 days. Figure 2(c) shows that the concentration of GP also increased significantly in the acute phase but then showed a slow upward trend. As the injury time increased, the concentration difference between the 30s-compressed group and the 120s-compressed group gradually decreased, which indicates that the difference in GP concentration caused by the degree of injury would gradually decrease over time.

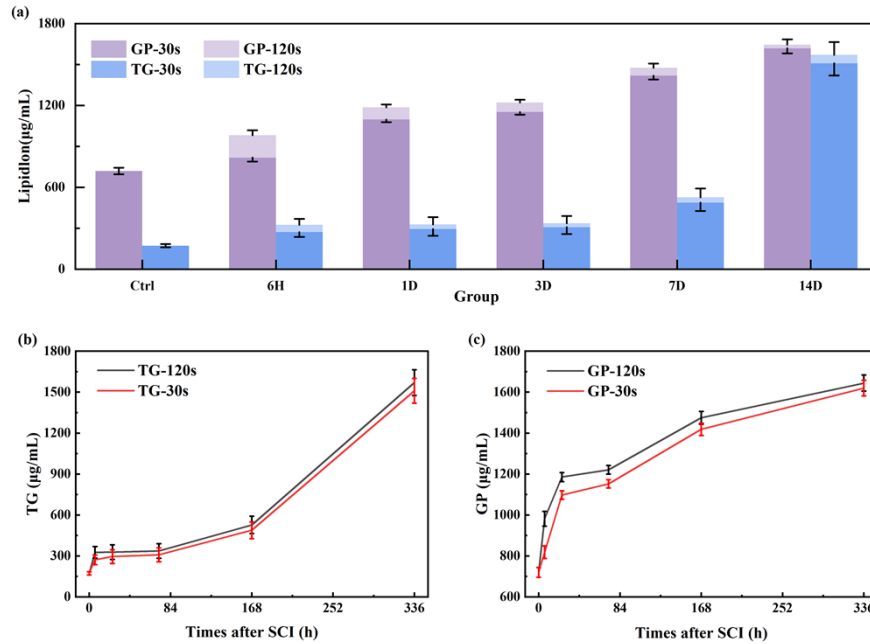


Fig. 2. Changes of GP and TG concentration in serum. (a) Histogram of GP and TG concentration; (b) The change of TG concentration with injury time and degree; (c) The change of GP concentration with injury time and degree.

4.2. THz-spectroscopy

Commonly, though, no reliable terahertz data is available below 50 to 100 GHz due to both the working range of the photomixers and parasitic interference effects prevalent at low frequencies. As a result, we chose the 300–1200 GHz band of the original spectrum as the frequency range for spectral analysis. Lowess smoothing is used to decrease the noise interference of spectral data. Since the system is easily disturbed by the external environment during operation, such as minor vibrations in the laboratory environment and potential power fluctuations in the laser used in the experiment, numerous measurements on the same sample are required to assure measurement accuracy and remove anomalous data. In our trials, each sample was evaluated five times, and the outliers were removed by the boxplot method. Figure 3 depicts the attenuated total reflectance spectrum measurement result of one of the healthy mouse serums, and it can be observed that the spectrum of the fourth measurement is much greater in the high-frequency region than the other four measurements. The box plot of the data at 1.1 THz also shows that the measured value of the fourth time much surpasses the 1.5 times quartile, indicating that it is an outlier for this type of data. Finally, relatively accurate measurement results are obtained by averaging the measurement data without anomalous data.

The calculated terahertz absorption coefficient and refractive index spectra are shown in Fig. 4. The shaded regions represent the standard error for each frequency point. As the frequency increases, the absorption coefficient of the serum continually increases while the refractive index

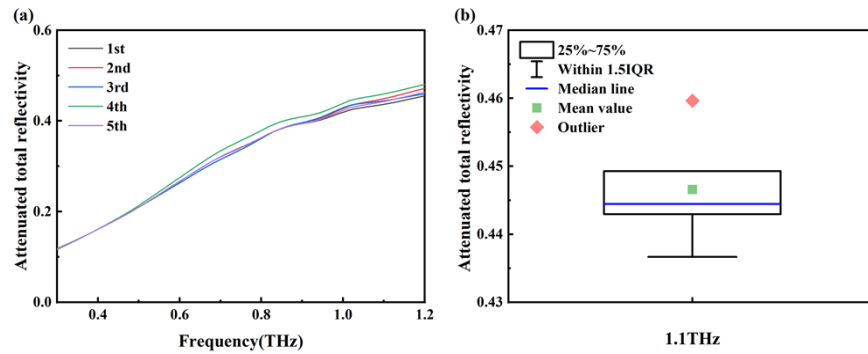


Fig. 3. Process of removing outliers from spectral data. (a) reduplicative ATR reflectivity spectra of a serum sample from control group; (b) boxplot based on the ATR reflectivity at 1.1 THz.

gradually decreases. The difference between the groups is not obvious at low frequencies, but at 0.9–1.2 THz, the refractive index of the SCI group's serum samples is significantly lower than that of the control group, and the refractive index of the samples decreases as the injury time increases. For the samples collected at the same time points, the longer the spinal cord is compressed, the smaller the refractive index is. At the same time, the absorption coefficient was shown to be positively associated with the time and severity of the injury. It is worth mentioning that the effect of spinal cord compression time on the refractive index of blood samples was less than that of damage time. The above analysis shows that the THz spectrum can sensitively reflect the changes in degree and time of SCI in rats.

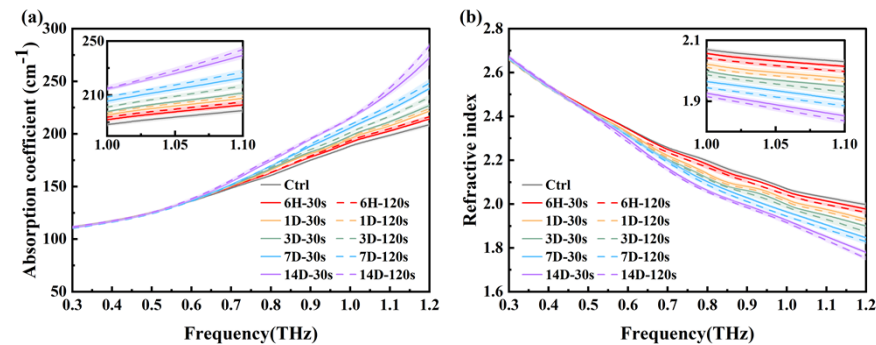


Fig. 4. THz spectra of serum. (a) Absorption coefficient spectra of serum; (b) Refractive index spectra of serum. Ctrl, 6H, 1D, 3D, 7D and 14D represents the sham operation control group and the serum samples collected at 6 hours, 1 day, 3 days, 7 days and 14 days after SCI.

According to the above results, there is a certain negative correlation between the refractive index of serum measured by THz spectroscopy and the lipid concentration. To investigate their functional relationship further, PCA and LSR algorithms are used to identify and classify the THz refractive index spectrum of serum. Since the impact of the injury time on the spectral refractive index is much smaller than that of the damage time, the spectral data of the compression times of 30s and 120s were combined into one group for classification purposes; thus, six groups of data under different time points are obtained; each group contained six serum samples. It is necessary to reduce the dimensionality of the spectral data to remove redundant information. PCA is a classic approach for data dimensionality reduction by employing a small number of

principal components to explain the covariance structure of the original data, thus PCA was initially used to reduce the dimensionality of the data. In our experiments, the PCA algorithm was implemented using MATLAB software, and its main steps include zero-mean matrix construction, covariance matrix calculation, eigenvalues and eigenvectors computation, component matrix construction, and data dimensionality reduction. When reducing the data's dimensionality, the component matrix is constructed using the top 'n' eigenvectors, where 'n' is a positive integer. The choice of 'n' is related to the contribution of principal components to the variance. In our experiments, selecting 'n' as 30 achieved effective dimensionality reduction. Figure 5(a) shows the eigenvalues of the first five principal components (PCs) and their cumulative contributions to the total variance of the data. As the number of PCs increased, the eigenvalues decreased rapidly; the first PC and the second PC accounted for 97.9% and 1.4% of the total variance of the serum spectral data, respectively, while the other PCs accounted for less than 1% of the total variance of the data. It indicated that the first two PCs already included the majority of the spectral data characteristics. Figure 5(b) shows the scores of the first two PCs. The samples are divided into six groups according to the time of SCI, and the confidence ellipse for each group of data is drawn based on the 95% confidence interval. The scatter plot shows that the six groups of samples have good clustering properties, especially for the first PC score of each group of data, which tends to grow as injury time increases. However, there was no significant difference between the groups in the second PC score. According to the above conclusions, we can establish the functional relationship between spectral data and serum lipid concentration based on the score of PC1.

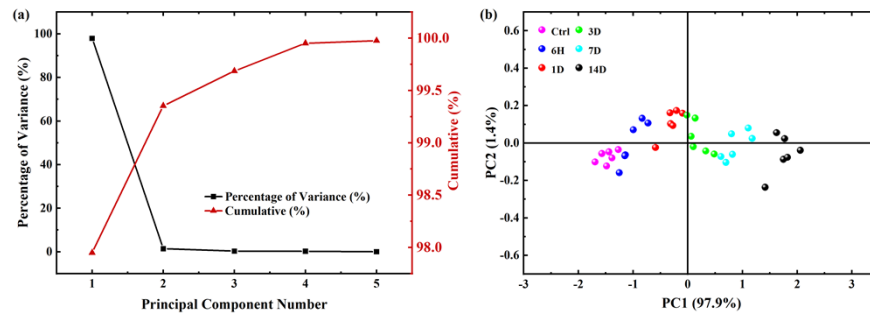


Fig. 5. Analysis results of PCA. (a) Cumulative and percentage of variance of the first 5 PCs; (b) Scores of serum samples on the first two PCs.

Based on the LSR algorithm, the regression equations between the PC1 score and the concentrations of GP and TG in serum were established. The linear function was applied to fit the regression equation between the GP concentration and PC1 score because their scatter distributions were approximately linearly correlated. The fitting result is shown in Fig. 6(a), where the 95% confidence band and 95% prediction band were drawn. The linear regression model has a very high correlation coefficient value ($R = 0.979$), which indicates that the linear regression model can accurately describe the relationship between the spectral PC1 scores and the concentration of GP in serum. For TG, because the scatter distribution of its concentration and PC1 scores resembles the exponential distribution, we fit the regression equation between TG concentration and PC1 scores through an exponential function, Fig. 6(b) depicts the results. In comparison to GP, the R-value of the fitting results for TG is relatively low ($R = 0.942$).

In addition to the R values, the performance of the LSR model was also evaluated by the root-mean-square standardized error of calibration (RMSSEC), root-mean-square standardized error of cross-validation (RMSSECV) and root-mean-square standardized error of prediction (RMSSEP). Correlation statistics are shown in Fig. 7, for GP, lower RMSSEC (0.70), lower RMSSECV (1.46), and lower RMSSEP (1.20) have been observed. Compared with GP, the

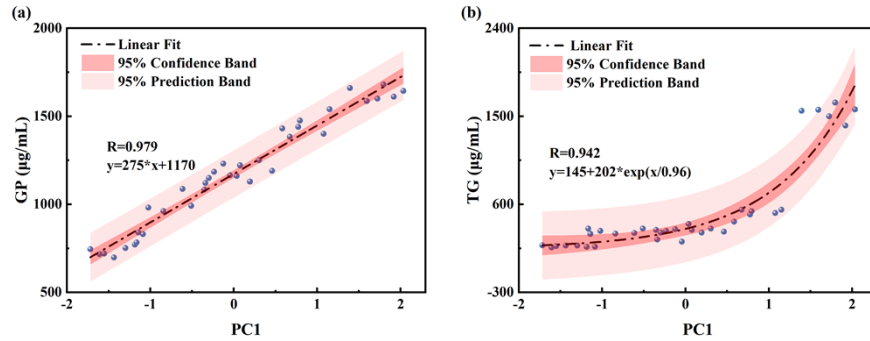


Fig. 6. The correlation between the scores of PC1 and GP/TG concentrations. (a) The linear correlation between the scores of PC1 and GP concentrations; (b) The exponential correlation between the scores of PC1 and TG concentrations.

relatively higher RMSSEC (2.23), RMSSECV (7.61), RMSSEP (25.17) and lower R values can be attributed to the fact that the concentration of TG at 14 days surged to three times that at 7 days, resulting in a paucity of sample data with a concentration between 600 and 1300 $\mu\text{g/mL}$. The results indicate that THz spectral characteristics have a better correlation with the concentration of GP, which enables the detection of concentrations of GP in serum by terahertz spectroscopy, in our research, the average detection accuracy is 94% based on the LSR model.

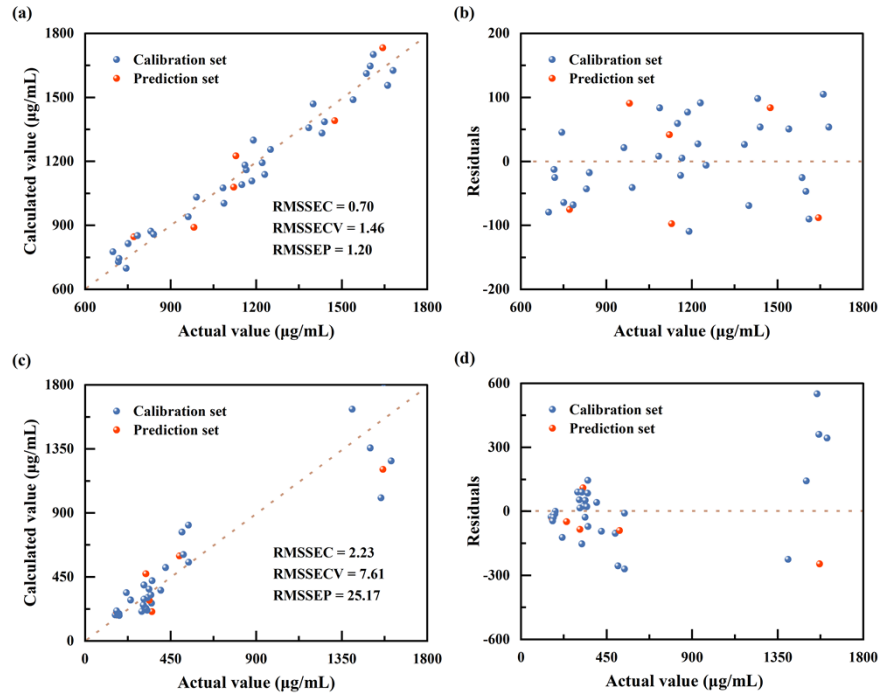


Fig. 7. Correlation statistics between calculated values and actual values using LSR algorithms. (a) Scatter distribution between the actual value and the calculated value of the concentrations of GP; (b) Prediction residuals for concentrations of GP; (c) Scatter distribution between the actual value and the calculated value of the concentrations of TG; (d) Prediction residuals for concentrations of TG.

5. Conclusion

In this paper, based on THz-ATR-FDS with optical hybrid coherent detection, the terahertz spectra (0.3–1.2 THz) of rat serum samples with different injury degrees and different time nodes after SCI were measured. The results reveal that the spectral characteristics can sensitively reflect the changes in injury time and degree, which are correlated positively with the THz spectral absorption coefficient and negatively with the refractive index. To further investigate the pathogenesis of SCI, we examined the changes in serum lipid concentration at different time points following different injury degrees and discovered that the concentration of GP and TG increased with the time and degree of injury. Finally, based on PCA and the LSR algorithm, we established the regression equation between THz spectral characteristics of serum and GP/TG concentrations, the correlation coefficients were both greater than 0.94 and the average detection accuracy of concentration is 94%, which indicated that terahertz spectroscopy could accurately detect changes in serum lipid concentration caused by SCI. Therefore, this study provides a high-resolution, efficient, and label-free clinical application strategy for the detection of SCI as well as the long-term monitoring of blood lipid content in SCI patients.

However, due to the limitations of the current detection equipment, we have now only employed a mass spectrometry for the concentration measurement of lipid molecules in serum. To understand the specific reasons behind the variations in terahertz spectroscopic parameters, a more in-depth and comprehensive investigation of other molecular components in serum, such as proteins and sugars, will be a focal point of our future research efforts. Additionally, the relatively small sample size chosen in this study may also contribute to the limitations in the accuracy of concentration predictions. Therefore, in future research, the inclusion of larger sample sizes and the utilization of more advanced and efficient prediction algorithms will be necessary.

Funding. National Key Research and Development Program of China (2022YFB2903800); “Pioneer” and “Leading Goose” R&D Program of Zhejiang (2023C01139); National Natural Science Foundation of China (62101483); Natural Science Foundation of Zhejiang Province (LQ21F010015, LY21H060005).

Disclosures. The authors declare that there are no conflicts of interest related to this article.

Data availability. Data underlying the results presented in this paper are not publicly available at this time but may be obtained from the authors upon reasonable request.

References

1. P. A Ball, “Critical care of spinal cord injury,” *Spine* **26**(Supplement), S27–S30 (2001).
2. A Alizadeh, M Dyck S, and S Karimi-Abdolrezaee, “Traumatic spinal cord injury: an overview of pathophysiology, models and acute injury mechanisms,” *Front. Neurol.* **10**, 282 (2019).
3. S. L. James, A. Theadom, R. G. Ellenbogen, *et al.*, “Global, regional, and national burden of traumatic brain injury and spinal cord injury, 1990–2016: a systematic analysis for the Global Burden of Disease Study 2016,” *Lancet Neurol.* **18**(1), 56–87 (2019).
4. C. S. Ahuja, J. R. Wilson, S. Nori, *et al.*, “Traumatic spinal cord injury,” *Nature reviews Disease primers* **3**(1), 17018 (2017).
5. Y Mao, T Nguyen, T Sutherland, *et al.*, “Endogenous neural progenitor cells in the repair of the injured spinal cord,” *Neural Regener. Res.* **11**(7), 1075 (2016).
6. G Li, Y Cao, F Shen, *et al.*, “Mdivi-1 inhibits astrocyte activation and astroglial scar formation and enhances axonal regeneration after spinal cord injury in rats,” *Front. Cell. Neurosci.* **10**, 241 (2016).
7. Z Li, T Zhao, J Ding, *et al.*, “A reactive oxygen species-responsive hydrogel encapsulated with bone marrow derived stem cells promotes repair and regeneration of spinal cord injury,” *Bioact. Mater.* **19**, 550–568 (2023).
8. B Acheson M, R Livingston R, L Richardson M, *et al.*, “High-resolution CT scanning in the evaluation of cervical spine fractures: comparison with plain film examinations,” *AJR, Am. J. Roentgenol.* **148**(6), 1179–1185 (1987).
9. R Vaccaro A, D Koerner J, E Radcliff K, *et al.*, “AOSpine subaxial cervical spine injury classification system,” *European spine journal* **25**(7), 2173–2184 (2016).
10. D Lammertse, D Dungan, J Dreisbach, *et al.*, “Neuroimaging in Traumatic Spinal Cord Injury: An Evidence-based Review for Clinical Practice and Research: Report of the National Institute on Disability and Rehabilitation Research Spinal Cord Injury Measures Meeting,” *J. Spinal Cord Med.* **30**(3), 205–214 (2007).
11. A Curt and V Dietz, “Electrophysiological recordings in patients with spinal cord injury: significance for predicting outcome,” *Spinal cord* **37**(3), 157–165 (1999).

12. Z Yang, M Bramlett H, A Moghieb, *et al.*, "Temporal profile and severity correlation of a panel of rat spinal cord injury protein biomarkers," *Mol. Neurobiol.* **55**(3), 2174–2184 (2018).
13. CA Oyinbo, "Secondary injury mechanisms in traumatic spinal cord injury: a nugget of this multiply cascade," *Acta Neurobiol. Exp.* **71**(2), 281–299 (2011).
14. MA Anwar, TS Al Shehabi, and AH Eid, "Inflammogenesis of secondary spinal cord injury," *Front. Cell. Neurosci.* **10**, 98 (2016).
15. A Bauman W and M Spungen A, "Invited review carbohydrate and lipid metabolism in chronic spinal cord injury," *J. Spinal Cord Med.* **24**(4), 266–277 (2001).
16. I Pineau and S Lacroix, "Proinflammatory cytokine synthesis in the injured mouse spinal cord: Multiphasic expression pattern and identification of the cell types involved," *J. Comp. Neurol.* **500**(2), 267–285 (2007).
17. Y Wu, F Streijger, Y Wang, *et al.*, "Parallel metabolomic profiling of cerebrospinal fluid and serum for identifying biomarkers of injury severity after acute human spinal cord injury," *Sci. Rep.* **6**(1), 38718 (2016).
18. J Halford, S Shen, G Itamura, *et al.*, "New astroglial injury-defined biomarkers for neurotrauma assessment," *J. Cereb. Blood Flow Metab.* **37**(10), 3278–3299 (2017).
19. X Yang, X Zhao, K Yang, *et al.*, "Biomedical applications of terahertz spectroscopy and imaging," *Trends Biotechnol.* **34**(10), 810–824 (2016).
20. Z Yan, G Zhu L, K Meng, *et al.*, "THz medical imaging: from in vitro to in vivo," *Trends Biotechnol.* **40**(7), 816–830 (2022).
21. M Zhang and T W Yeow J, "Nanotechnology-Based Terahertz Biological Sensing: A review of its current state and things to come," *IEEE Nanotechnology Mag.* **10**(3), 30–38 (2016).
22. J Neu and A Schmittenmaer C, "Tutorial: An introduction to terahertz time domain spectroscopy (THz-TDS)," *J. Appl. Phys.* **124**(23), 1 (2018).
23. L Liebermeister, S Nellen, B Kohlhaas R, *et al.*, "Optoelectronic frequency-modulated continuous-wave terahertz spectroscopy with 4 THz bandwidth," *Nat. Commun.* **12**(1), 1071 (2021).
24. Y Kong D, J Wu X, B Wang, *et al.*, "High resolution continuous wave terahertz spectroscopy on solid-state samples with coherent detection," *Opt. Express* **26**(14), 17964–17976 (2018).
25. S Fan, P J Parrott E, S Y Ung B, *et al.*, "Calibration method to improve the accuracy of THz imaging and spectroscopy in reflection geometry," *Photonics Res.* **4**(3), A29–A35 (2016).
26. D Suhandy, T Suzuki, Y Ogawa, *et al.*, "A quantitative study for determination of sugar concentration using attenuated total reflectance terahertz (ATR-THz) spectroscopy," *Sensing for Agriculture and Food Quality and Safety III* **5**(3), 90–95 (2012).
27. H Hirori, K Yamashita, M Nagai, *et al.*, "Attenuated total reflection spectroscopy in time domain using terahertz coherent pulses," *Jpn. J. Appl. Phys.* **43**(10A), L1287–L1289 (2004).
28. Y Wang, G Wang, D Xu, *et al.*, "Terahertz spectroscopic diagnosis of early blast-induced traumatic brain injury in rats," *Biomed. Opt. Express* **11**(8), 4085–4098 (2020).